



LABORATORI NAZIONALI DI FRASCATI

SIS-Pubblicazioni

LNF-04/07

NEUTRINO OSCILLATION STUDIES WITH LASER-DRIVEN BEAM DUMP FACILITIES

S.V. Bulanov^{1,5}, T. Esirkepov^{1,6}, P. Migliozzi², F. Pegoraro³, T. Tajima¹, F. Terranova⁴

¹⁾ *Kansai Research Establishment, JAERI, Japan.*

²⁾ *INFN, Sez. di Napoli, Napoli, Italy*

³⁾ *Dip. di Fisica, Univ. di Pisa and INFN, Pisa, Italy*

⁴⁾ *INFN, Laboratori Nazionali di Frascati, Frascati, Italy*

⁵⁾ *A. M. Prokhorov Institute of RAS, Moscow, Russia*

⁶⁾ *Moscow Institute of Physics and Technology, Dolgoprudny, Russia.*

Abstract

A new mechanism is suggested for efficient proton acceleration in the GeV energy range; applications to non-conventional high intensity proton drivers and, hence, to low-energy (10-200 MeV) neutrino sources are discussed. In particular we investigate possible uses to explore subdominant $\bar{\nu}_\mu \rightarrow \bar{\nu}_e$ oscillations at the atmospheric scale and their CP conjugate. We emphasize the opportunity to develop these facilities in conjunction with projects for inertial confined nuclear fusion and neutron spallation sources.

PACS: 14.60.Pq, 52.38.Kd, 41.75.Lx

1 Introduction

In the light of the strong evidence [1] for neutrino oscillations coming from atmospheric and solar neutrino experiments, recently corroborated by reactor and accelerator results, a very peculiar texture of the leptonic mixing matrix is emerging. Current results point towards two hierarchical mass scale differences¹ ($\Delta m_{12}^2 \ll |\Delta m_{13}^2| \simeq |\Delta m_{23}^2|$) driving, respectively, the oscillations at the “solar” and “atmospheric” scales. The corresponding mixing angles are large but the interference between the two scales (sub-dominant $\nu_\mu \rightarrow \nu_e$ oscillations at $E/L \sim |\Delta m_{23}^2|$, L and E being the neutrino path-length and energy) has never been observed [2,3]. The leptonic mixing matrix (Pontecorvo-Maki-Nakagawa-Sakata, PMNS [4]) is usually parametrized [5] as:

$$U(\theta_{12}, \theta_{13}, \theta_{23}, \delta) = \begin{pmatrix} c_{12}c_{13} & s_{12}c_{13} & s_{13} \\ -s_{12}c_{23} - c_{12}s_{23}s_{13}e^{i\delta} & c_{12}c_{23} - s_{12}s_{23}s_{13}e^{i\delta} & s_{23}c_{13}e^{i\delta} \\ s_{12}s_{23} - c_{12}c_{23}s_{13}e^{i\delta} & -c_{12}s_{23} - s_{12}c_{23}s_{13}e^{i\delta} & c_{23}c_{13}e^{i\delta} \end{pmatrix} \quad (1)$$

with $s_{ij} = \sin \theta_{ij}$ and $c_{ij} = \cos \theta_{ij}$; current data suggest [6] at 90% confidence level $35^\circ < \theta_{23} < 55^\circ$, $\theta_{12} = 32.5^\circ \pm 2.4^\circ$ and small values for θ_{13} ($\lesssim 10^\circ$) i.e. support a “bi-large” PMNS. In fact, in the limit $\theta_{13} \rightarrow 0$ the matrix becomes real-valued and the complex CP violating phase turns out to be unobservable. It follows that the possibility to determine experimentally the (1, 3) sector of PMNS - i.e. the off-diagonal factor $U_{e3} \equiv s_{13}e^{-i\delta}$ - and, in particular, the Dirac phase δ critically depends on the size of θ_{13} . No theoretical inputs are available to constrain the size of θ_{13} and δ in a convincing manner, so that its experimental determination is mandatory. Such determination can be carried out at accelerators either measuring the size of the subdominant $\nu_\mu \rightarrow \nu_e$ ($\bar{\nu}_\mu \rightarrow \bar{\nu}_e$) oscillation probability at the atmospheric scale or its T-conjugate $\nu_e \rightarrow \nu_\mu$ ($\bar{\nu}_e \rightarrow \bar{\nu}_\mu$). This measure will likely be the most challenging task of future long-baseline neutrino oscillation experiments and, for θ_{13} values significantly smaller than current limits, traditional accelerating techniques will be unable to provide the requested intensity and purity. Therefore, interest for unconventional neutrino sources has steadily grown in recent years, bringing e.g. to the proposals of the Neutrino Factories [7] or the Beta-beams [8].

Along this line, in this paper we consider a wide synergic scenario between nuclear and neutrino physics programs connecting the long term development of facilities for laser-driven inertial confinement fusion (ICF) and the possibility to obtain an ultra-intense low-energy (1-2 GeV) proton driver for neutrino studies and spallation neutron

¹We assume here only three active neutrinos with masses m_1 , m_2 and m_3 ; hence, only two independent mass scale differences exist ($\Delta m_{12}^2 \equiv m_2^2 - m_1^2$ and $\Delta m_{23}^2 \equiv m_3^2 - m_2^2$) since $\Delta m_{13}^2 = \Delta m_{23}^2 + \Delta m_{12}^2$.

sources (see Appendix). Such a link is made possible if an efficient laser-based acceleration mechanism is available in the near future. This mechanism is described in details in Sec. 2. The connection with neutrino physics results from the following consideration. Sources of neutrinos with energy beyond the μ production threshold in ν_μ charged-currents (CC) interactions are not strictly necessary to explore the magnitude and phase of U_{e3} . In principle, a high intensity source of ν_μ and $\bar{\nu}_\mu$ with energy of the order of a few tens of MeV would suffice to search for $\nu_\mu \rightarrow \nu_e$ appearance and its CP-conjugate at baselines of $L \sim 10$ km. The neutrinos come from pion and muon decays at rest (DAR) and the pions can be produced by a high current proton beam dump facility. These beams, if available with proper intensity would provide *simultaneously* a source for $\nu_\mu \rightarrow \nu_e$ oscillations through the $\pi^+ \rightarrow \mu^+ \nu_\mu$ DAR chain and a source for $\bar{\nu}_\mu \rightarrow \bar{\nu}_e$ through the subsequent $\mu^+ \rightarrow e^+ \bar{\nu}_\mu \nu_e$ decay. Moreover, differently from Superbeams [9,10], the intrinsic ν_e ($\bar{\nu}_e$) beam contamination can be kept easily below 0.1% (see Sec. 3), as the facility can be operated below the K production threshold.

The acceleration of protons up to several tens of MeV by the interaction of ultra-intense laser beams with solid targets has been recently reported by several experiments [11]. This process will probably open up a wealth of applications: radioisotope production [12], proton probing [13] and oncological hadron-therapy [14] have been discussed. Moreover, the laser-driven acceleration mechanism is a natural candidate for fast beam injection into conventional accelerators [15]. Part of these research programs might be carried out already with present laser technologies, provided that a suitable repetition rate, reproducibility and an improved beam quality become available. On the other hand, future developments towards higher laser intensities [16,17] would allow particle acceleration for High Energy Physics applications.

In fact, laser-driven acceleration mechanisms mainly favor applications that profit of the significant beam intensity without imposing strong constraints on the beam quality (energy spread and emittance) and particle energy. The possibility of using the well-controlled time structure of laser-induced ν beams to test the KARMEN time anomaly or increasing the laser intensity to overcome the kinematical threshold for muon production (ν_μ disappearance tests) has already been considered in [18]. The pion generation by the laser accelerated ions has also been discussed in [19]. Similarly, in this paper we suggest that the above-mentioned technique could be implemented to overcome the present limitations of proton dump facilities (Sec. 2) and, particularly, high intensity DAR neutrino beams (Sec. 3). We investigate its capability to clarify the (1,3) sector of the PMNS matrix, with emphasis on the size of θ_{13} (Sec. 4-6), and the main technological challenges for a new generation of beam dump facilities.

2 Laser ion accelerators

The classical mechanism of ion acceleration through the interaction of a laser pulse with a plasma target is a direct consequence of the electron acceleration. Due to the smaller electron mass, the energy of the laser light is first transformed into electron kinetic energy. The resulting displacement of the electrons and the modification of their density lead to the formation of a region with a strong electric charge separation. This causes an intense electric field which eventually accelerates the ions. In the simplest case of a one-dimensional geometry, when a transversally wide laser pulse interacts with a thin foil, the ponderomotive pressure of the laser pulse shifts the electrons with respect to ions, forming a strong electric field layer between the two species. An electric field also can be formed due to charge separation if the laser radiation accelerates a relatively large portion of the electrons, expelling them almost isotropically. In this case the fast electrons leave the targets and the heavier ions remain at rest forming extended regions of positive electric charge. Then the ions with non-compensated electric charge expand and acquire a kinetic energy. This corresponds to the so called “Coulomb explosion” regime. In configurations with more than one dimensions, different effects come into play such as the finite size of the waist of the laser beam, the transverse filamentation instability of a wide electromagnetic packet in a plasma, and the transverse modulations of the electron and ion layers. These effects usually reduce the energy of the fast ions and/or the efficiency of the energy transformation compared to the one obtained within the framework of the one-dimensional approximation.

However, the process of ion acceleration exhibits new properties in the regime where the radiation pressure of the electromagnetic wave plays a dominant role in the laser-foil interaction, as demonstrated in Refs. [17,20]. In this regime electrons gain their energy due to the radiation pressure in a way that, qualitatively, resembles the ion acceleration mechanism proposed by Veksler [21] in 1956. Here, the ion component moves forward with almost the same velocity as the average longitudinal velocity of the electron component, hence with a kinetic energy well above that of the electron component. The ion acceleration appears to be due to the radiation pressure of the laser light on the electron component with the momentum being transferred to the ions through the electric field arising from charge separation. This mechanism of ion acceleration can be called the Radiation Pressure Dominant (RPD) mechanism. In contrast to the schemes previously discussed in the literature (see e.g. [22–24]) here the ion beam generation is highly efficient, and, as we will see later on, the ion energy per nucleon is proportional to the laser pulse energy.

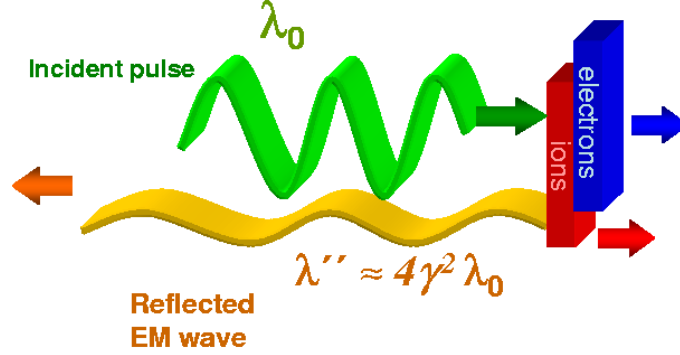


Figure 1: Interaction of the e.m. wave with the co-propagating proton-electron mirror.

2.1 Radiation Pressure-dominated (RPD) regime: 1D analytical description

The acceleration mechanism can be explained as follows. The accelerated foil, which consists of the electron and proton layers, can be regarded as a relativistic plasma mirror co-propagating with the laser pulse. Assume that the laser pulse is perfectly reflected from this mirror. As a result of the reflection at the co-propagating relativistic mirror, the frequency of the electromagnetic wave decreases by the factor of $(1 - v/c) / (1 + v/c) \approx 1/4\gamma^2$, where v is the mirror velocity and $\gamma = (1 - v^2/c^2)^{-1/2}$ is the Lorentz-factor of the plasma mirror².

Before the reflection, in the laboratory reference frame, the incident laser pulse energy $\mathcal{E}_{las,in}$ is proportional to $E_0^2 L_{las,in}$, where E_0 is the electric field amplitude and $L_{las,in}$ is the incident pulse length. After the reflection the pulse energy becomes much lower: $\mathcal{E}_{las,ref} \propto E_{las,ref}^2 L_{las,ref} \approx E_0^2 L_{las,in} / 4\gamma^2$. The length of the reflected pulse is longer by a factor $4\gamma^2$, and the electric field is smaller by a factor $4\gamma^2$. Hence the plasma mirror acquires the energy $(1 - 1/4\gamma^2)\mathcal{E}_{las,in}$ from the laser. In this stage the radiation pressure of the light accelerates the plasma slab (electrons and protons). As discussed above, the radiation momentum is transferred to the protons through the charge separation field and the kinetic energy of the protons is much greater than that of the electrons. This scenario is illustrated in Fig. 1, where a sketch of the e.m. wave interaction with the co-propagating proton-electron slab is presented.

It is possible to estimate the proton maximum energy and the acceleration efficiency

²To ease comparison with existing literature, we use here the Gaussian CGS system of unit ($c \neq 1$). We resume the usual $c = 1$ system in the subsequent sections.

using the model of the flat foil driven by the e.m. radiation pressure, as described above. The radiation pressure is given by:

$$P = \frac{E_0'^2}{2\pi} = \left(\frac{\omega'}{\omega}\right)^2 \frac{E_0^2}{2\pi} = \frac{E_0^2}{2\pi} \left(\frac{c-v}{c+v}\right), \quad (2)$$

where $v = dx/dt$ is the foil instantaneous velocity, i.e.

$$\frac{dx}{dt} = c \frac{p}{(m_p^2 c^2 + p^2)^{1/2}}. \quad (3)$$

Here primed (unprimed) quantities refer to the moving (laboratory) reference frame respectively. In a quasi-one-dimensional geometry, the laser electric field at the foil location $x(t)$ depends on time as $E_0' = E_0(t - x(t)/c)$.

Since the expression of the radiation pressure is the same in both frames, we can write the equation of motion of the foil as

$$\frac{dp}{dt} = \frac{E_0^2(t - x(t)/c)}{2\pi n_0 l_0} \frac{(m_p^2 c^2 + p^2)^{1/2} - p}{(m_p^2 c^2 + p^2)^{1/2} + p}, \quad (4)$$

where p is the momentum of the proton representing the foil, l_0 and n_0 are the thickness and initial proton density of the foil. In this approximation we neglect the heating of the proton fluid.

In the simplest case, when the laser pulse is assumed to be long enough and with a homogeneous amplitude, we can consider the electric field E_0 in Eq. (4) to be constant. Its solution $p(t)$ is an algebraic function of time t . For the initial condition $p = 0$ at $t = 0$ it can be written in the implicit form

$$\frac{2p^3 + 2(m_p^2 c^2 + p^2)^{3/2}}{3m_p^2 c^2} + p - \frac{2}{3}m_p c = \frac{E_0^2}{2\pi n_0 l_0} t. \quad (5)$$

At the initial stage, for $t \ll 2\pi n_0 l_0 m_p c / E_0^2$, the proton momentum is a linear function of time:

$$p \approx (E_0^2 / 2\pi n_0 l_0) t. \quad (6)$$

As $t \rightarrow \infty$, the dependence of the accelerated proton momentum on time changes asymptotically to

$$p \approx \mathcal{E}_{\text{pkin}} / c \approx m_p c (3E_0^2 t / 8\pi n_0 l_0 m_p c)^{1/3}. \quad (7)$$

We notice here the obvious analogy between the proton motion regime described by the expression (5) and the solution of the problem of the acceleration of a charged particle under the radiation pressure of the electromagnetic wave. This analogy can be clearly

seen by comparing Eq. (5) with the expression for the velocity of an accelerated electron, which, in this limit, can be cast in the form $\bar{W}\sigma_T t/m_e c \approx (2/3)(1 - v^2/c^2)^{3/2}$, with $c\bar{W} = cE_0^2/4\pi$ the wave intensity (see Ref. [25]), $\sigma_T = 8\pi r_e^2/3$ the Thomson cross section and $r_e = e^2/m_e c^2$ the classical electron radius. In our case $2/n_0 l_0$ plays the role of the effective cross section of the scattering of the electromagnetic wave. This analogy further underlines the similarity between the RPD mechanism of ion acceleration discussed here and the Veksler mechanism mentioned above.

To find an upper limit to the proton energy acquired during the interaction with a laser pulse of finite duration, we must include the dependence of the laser electromagnetic field on time t and on the coordinate x . Because of the foil motion, the interaction time can be much longer than the laser pulse duration $\tau_{las,in}$. We introduce the phase of the wave

$$\psi = \omega_0(t - x(t)/c), \quad (8)$$

as a new variable, ω_0 being the incoming laser frequency. Using Eq.(3) together with Eq.(8), we cast Eq.(4) for the particle momentum to the form

$$\frac{dp}{d\psi} = \frac{E_0^2(\psi)}{2\pi\omega_0 n_0 l_0} \frac{(m_p^2 c^2 + p^2)^{1/2}}{(m_p^2 c^2 + p^2)^{1/2} + p}. \quad (9)$$

Its solution reads

$$p = m_p c \frac{w(w+1)}{(w+1/2)}, \quad (10)$$

where w is a function of ψ :

$$w(\psi) = \int_{-\infty}^{\psi} \frac{E_0^2(s)}{4\pi\omega_0 n_0 l_0 m_p c} ds. \quad (11)$$

Using Eqs.(8) and (10) we find the dependence of the foil coordinate on time and write the equations for t and x as functions of the variable ψ in the form

$$\begin{aligned} \frac{dt}{d\psi} &= \frac{1}{\omega_0} \left(\frac{c}{c-v} \right) = \frac{1}{\omega_0} \frac{(m_p^2 c^2 + p^2)^{1/2}}{(m_p^2 c^2 + p^2)^{1/2} - p} \\ &= \frac{1}{\omega_0} [1 + 2w(w+1)] \end{aligned} \quad (12)$$

and

$$\frac{dx}{d\psi} = \frac{dx}{dt} \frac{dt}{d\psi} = \frac{c}{\omega_0} 2w(w+1). \quad (13)$$

For a constant amplitude laser pulse with $E_0^2(\psi) = E_0^2 \theta(\psi)$, where $\theta(\psi) = 0$ for $\psi < 0$ and $\theta(\psi) = 1$ for $\psi > 0$ is the unit step function, we have $w(\psi) = w_0 \theta(\psi) \psi$, with

$w_0 = E_0^2/(4\pi\omega_0 n_0 l_0 m_p c)$. Then Eqs. (12) and (13) yield the parametric dependence of the accelerated foil coordinate on time

$$t = (\psi + w_0\psi^2 + 2w_0^2\psi^3/3)/\omega_0, \quad (14)$$

$$x = (w_0\psi^2 + 2w_0^2\psi^3/3)(c/\omega_0). \quad (15)$$

In the limit $t \ll 2\pi n_0 l_0 m_p c/E_0^2$ we have $x \approx cw_0 t^2/\omega_0$, and for $t \rightarrow \infty$, $x \approx ct$, while the momentum p increases according to Eq. (7).

The function $w(\psi)$ given by Eq. (11) can be interpreted as the normalized energy of the portion of the laser pulse that has interacted with the moving foil by time t . Its maximum value is $w_{\max} = \mathcal{E}_{las,in}/\mathcal{N}_p m_p c^2$, where

$$\mathcal{E}_{las,in} = \frac{E_0^2 S c \tau_{las,in}}{4\pi} \quad (16)$$

is the laser pulse energy, $\mathcal{N}_p = n_0 l_0 S$ is the number of protons in the region, with area equal to S , of the foil irradiated by the laser pulse.

From the solution of Eq. (4) given by Eq. (10) in terms of w we obtain for the kinetic energy of a proton initially at rest

$$\mathcal{E}_{pkin} \equiv (m_p^2 c^2 + p^2)^{1/2} c - m_p c^2 = m_p c^2 w^2 / (w + 1/2). \quad (17)$$

In the limits $w \ll 1$ and $w \gg 1$, we have respectively

$$\mathcal{E}_{pkin} \approx 2m_p c^2 w^2, \quad \text{and} \quad \mathcal{E}_{pkin} \approx m_p c^2 w. \quad (18)$$

The upper limit to the proton kinetic energy and, correspondingly, to the efficiency of the laser-to-proton energy transformation can be obtained from Eq. (17) by setting $w = w_{\max} = \mathcal{E}_{las,in}/\mathcal{N}_p m_p c^2$:

$$\mathcal{E}_{pkin,max} = \frac{2\mathcal{E}_{las,in}}{2\mathcal{E}_{las,in} + \mathcal{N}_p m_p c^2} \frac{\mathcal{E}_{las,in}}{\mathcal{N}_p}. \quad (19)$$

We see that within this model almost all the energy of the laser pulse is transformed into the energy of the protons if $\mathcal{E}_{las,in} \gg \mathcal{N}_p m_p c^2/2$:

$$\mathcal{E}_{pkin,max} \simeq \frac{\mathcal{E}_{las,in}}{\mathcal{N}_p} \simeq \frac{E_0^2 c \tau_{las,in}}{4\pi n_0 l_0}. \quad (20)$$

It is worth noting that, when the RPD mechanism takes place, the dependence of the proton kinetic energy on the laser intensity and duration turns out to be linear. Moreover,

$\mathcal{E}_{p\text{kin,max}}$ does not depend on the size of the illuminated area S : within this simplified one-dimensional approximation, an increase of the focal spot S and the laser energy $\mathcal{E}_{\text{las,in}}$ that keep constant the ratio

$$\frac{\mathcal{E}_{\text{las,in}}}{S} = \frac{E_0^2 c \tau_{\text{las,in}}}{4\pi} \quad (21)$$

result in an increase of the number of accelerated protons $\mathcal{N}_p = n_0 l_0 S$ without perturbing the proton energy spectrum. The acceleration length $x_{\text{acc}} \approx c t_{\text{acc}}$ and the acceleration time t_{acc} can be estimated using Eq.(20) and the $t^{1/3}$ asymptotic dependence of the proton energy on time in Eq.(14) as

$$t_{\text{acc}} \approx \frac{2}{3} \left(\frac{\mathcal{E}_{\text{las,in}}}{\mathcal{N}_p m_p c^2} \right)^2 \tau_{\text{las,in}}. \quad (22)$$

2.2 Computer Simulations

Within the framework of the simplified 1D approximation used above, the protons formally have a monoenergetic spectrum. A number of processes such as the transverse inhomogeneity of the amplitude of the laser pulse, the electron stochastization due to “vacuum heating” [26] and the subsequent proton layer expansion under the action of the Coulomb repelling force may result in the broadening of the proton energy spectrum or in inefficient acceleration.

In order to examine this scheme in a three-dimensional geometry, whose effects can indeed play a crucial role in the dynamics and stability of the plasma layer under the action of a relativistically strong laser pulse, we have performed³ 3D particle-in-cell (PIC) simulations with the code REMP (Relativistic Electro-Magnetic Particle-mesh code). This code is based on the current assignment scheme “Density decomposition” [27]. In these simulations the laser pulse is linearly polarized along the z -axis and propagates in the direction of the x -axis. Its dimensionless amplitude is $a \equiv eE_0/m_e\omega c = 316$, corresponding to the peak intensity $I = 1.37 \times 10^{23} \text{ W/cm}^2 \times (1 \mu\text{m}/\lambda)^2$, $\lambda = 1 \mu\text{m}$ being the laser wavelength. The laser pulse is almost Gaussian with FWHM size $8\lambda \times 25\lambda \times 25\lambda$ and a sharp front starting from $a = 100$; its energy is $\mathcal{E}_L = 10 \text{ kJ} \times (\lambda/1 \mu\text{m})^2$. Protons are generated from a $1 \mu\text{m}$ foil. In fact, due to the finite contrast of the laser, pulse pedestals reaching the target before the main pulse will pre-form a fully ionized plasma [28,29]. Therefore, in the present situation the target behaves as a fully ionized, 1λ thick plasma

³3D fully relativistic simulations of laser-plasma interactions represent major numerical efforts. The simulation under consideration has been performed on 720 processors of the supercomputer HP Alpha server SC ES40 at JAERI Kansai and form the basis of the studies of Refs. [17]. Here we make use of these results and, when appropriate, perform extrapolations to other flux and energy ranges. A more detailed numerical study is in progress and results will be presented in a forthcoming publication.

with density $n_e = 5.5 \times 10^{22} \text{ cm}^{-3} \times (1 \mu\text{m}/\lambda)^2$, which corresponds to the Langmuir frequency $\omega_{pe} = 7\omega$. The protons and the electrons have the same absolute charge and their mass ratio is $m_p/m_e = 1836$. The simulation box size is $100\lambda \times 72\lambda \times 72\lambda$ corresponding to the grid size $2500 \times 1800 \times 1800$, so the mesh size is 0.04λ . The total number of quasi-particles is 4.37×10^9 . The boundary conditions are periodic along the y - and z -axis and absorbing along the x -axis for both the e.m. radiation and the quasi-particles. The results of these simulations are shown in Figs. 2-5, where the space and time units are respectively the wavelength λ and period $2\pi/\omega$ of the incident radiation.

Fig. 2 shows the proton density and the E_z component of the electric field. We see that a region of the foil with the size of the laser focal spot is pushed forward. Although the plasma in the foil is overcritical, it is initially “transparent” for the laser pulse due to the effect of relativistic transparency (see e.g. [22]). Therefore a portion of the laser pulse passes through the foil. Eventually the pulse accelerates the electrons and, as a result of the charge separation, a longitudinal electric field is formed. This can be interpreted as the “rectification” of the laser light, by analogy with a rectifier in electrical engineering: the transverse oscillating electric field in the pulse is transformed into a longitudinal quasi-static electric field. The dimensionless amplitude of the longitudinal field is $a_{\parallel} \approx 150$ corresponding to $E_{\parallel} = 4.8 \times 10^{14} \text{ V/m} \times (1 \mu\text{m}/\lambda)$. The typical distance over which charge separation occurs is comparable with the initial thickness of the foil and is much smaller than the transverse size of the region that is being pushed. The proton layer is accelerated by this longitudinal field. We note that the laser pulse frequency in the reference frame comoving with the accelerated plasma region decreases as time progresses so that the accelerating foil become less transparent with time.

As seen in the cross-section of the electric field component E_z in Fig. 2, the thickness of coloured stripes, which corresponds to half of the radiation wave length, increases from left to right in the reflected part of the pulse (along the x -axis). This increase is weaker at the periphery (in the transverse direction). This ‘nonuniform red shift’ results from the Doppler effect when the laser light is reflected from the co-propagating relativistic mirror which accelerates and deforms in time. The red shift testifies that the laser pulse does indeed lose its energy by accelerating the plasma mirror. In this stage, the foil is transformed into a “cocoon” inside which the laser pulse is almost confined. The accelerated protons form a nearly flat “plate” at the front of the “cocoon” as is seen in Fig. 3.

Fig. 4 shows the maximum proton energy versus time. This dependence is initially linear and, at later times, the maximum proton energy scales as $t^{1/3}$ as predicted by the 1D analytical model of Sec. 2.1. The protons in the plate structure are accelerated according to the RPD regime. These results provide numerical evidence of the fact that the RPD

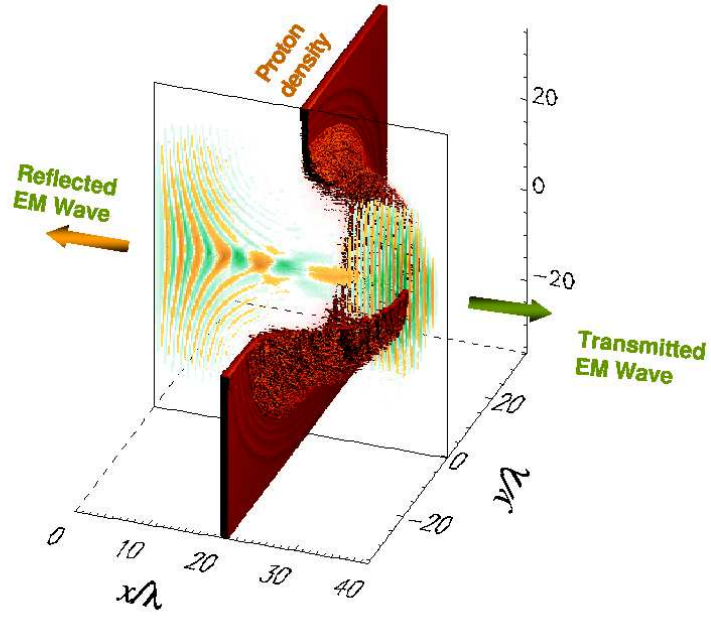


Figure 2: Spatial distribution of the proton density and the z component of the electric field during the acceleration phase (see text for details).

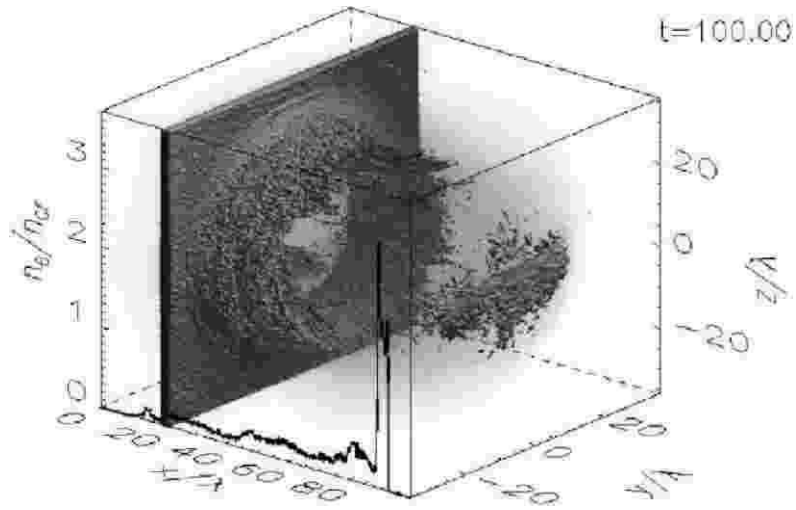


Figure 3: Spatial distribution of the proton density at $t = 100$.

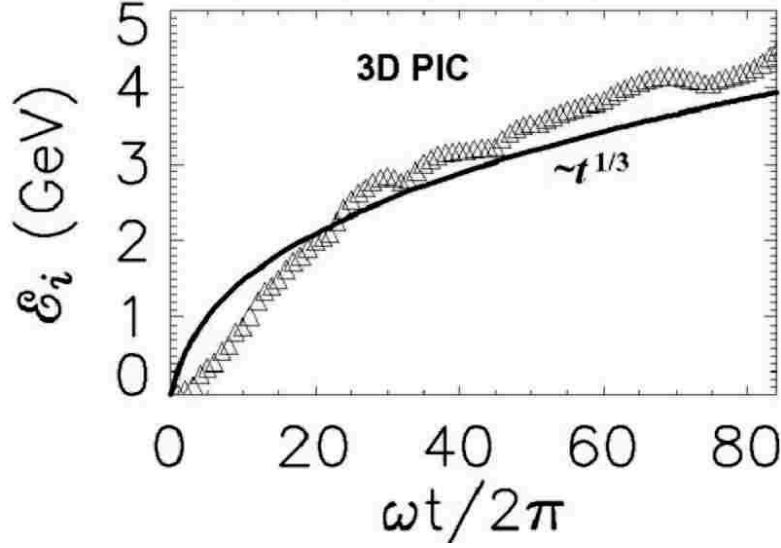


Figure 4: Maximum proton energy versus time. The continuous line represents the analytical expectation.

acceleration mechanism should appear already for laser intensities of 10^{23} W/cm². The time evolution is hydrodynamically stable and the acceleration highly efficient. In comparison with the experimental results of present day Petawatt lasers, this example predicts yet another astonishing advantage of the Exawatt lasers [16,30], besides those described in Refs. [16,31].

In Fig. 5 we show the proton energy distribution obtained in the 3D PIC simulations and their transverse emittance. The energy spectra have been calculated for the particles in the region near the beam axis (“plate”) within a $1\mu m$ radius. We see that the protons have a finite-width spectrum, localized within the interval $1.3 \text{ GeV} < \mathcal{E}_{pkin} < 3.2 \text{ GeV}$. The number of protons, integrated over energy, in the dashed region in Fig. 5 is equal to 2.7×10^{10} particles per μm^2 . The proton transverse emittance is almost constant and equals $\approx 10^{-2}\pi \text{ mm mrad}$.

The numerical studies depicted above are extremely challenging even for large parallel computer facilities. In order to reduce complexity, the study has been carried out with laser pulse of relatively small focal spot. In addition, the dynamical evolution has been followed up until the $t^{1/3}$ asymptotic behaviour is reached (i.e. before the complete laser-plasma decoupling). The overall laser energy to proton kinetic energy conversion efficiency (ϵ) at that time is 40%. Extrapolation up to the time of decoupling indicates that an energy conversion efficiency of 57% can be reached. On the other hand, due to

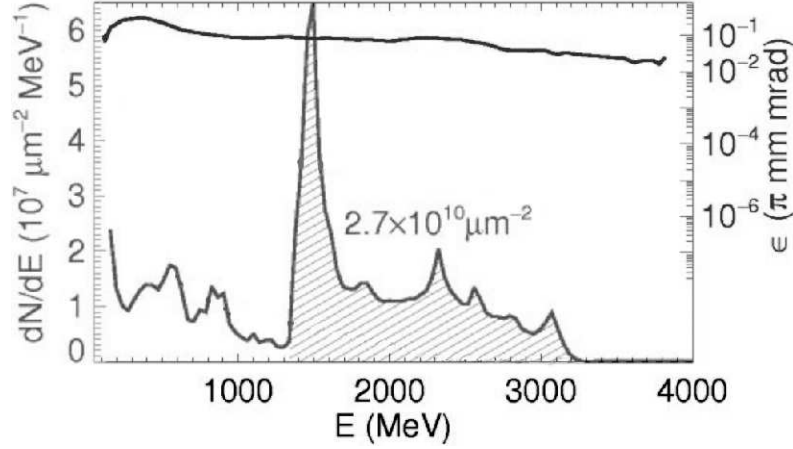


Figure 5: Proton energy distribution (red) and transverse emittance (blue) near the beam axis at $t = 80$.

the small focal spot, the RPD regime is operational only the central area: here a nearly-monochromatic spectrum is observed. The peripheral area (“cocoon”) result in a nearly-thermal spectrum of protons. Hence, if we consider only the RPD accelerated protons at time of decoupling, the efficiency drops to 11%. This value is the most conservative estimate of conversion efficiency and it is not expected to hold for large focal spots S : the “cocoon” is the outcome of a border effect due to the finite waist of the pulse and will not scale linearly with S . Finally, note that the intensity and the duration of the pulse has not been optimized for the production of protons in the few GeV range but has been chosen to demonstrate the possibility of highly relativistic ion generation [17]. Awaiting for further numerical studies, in the following sections the proton and neutrino fluxes are provided as a function of the repetition rate and realistic expectations are discussed below.

2.3 Proton fluxes

A proof of principle of the RPD acceleration mechanism is at the borderline of current technology, but the possibility of using this technique to overcome the limitation of traditional proton accelerators faces many additional difficulties. Present day systems based on Chirped Pulse Amplification [32] (CPA) are able to deliver intensities of the order of 10^{22} W/cm². It can be expected that the intensity needed to trigger the RPD mechanism will be reached in the near future since for intensities up to 10^{23} W/cm² the saturation fluence remains below the damage threshold and we can still profit of CPA for short-pulse generation. On the other hand, all present high power lasers operate at very low repetition

rate. This is a classical problem e.g. in inertial fusion: here, the basic principles could be demonstrated through the construction of optical cavities delivering up to 1.8 MJ as the National Ignition Facility (NIF) in US or the Laser Megajoule (LMJ) in France. However, the ultimate use of ICF to produce electric power will require repetition rates of the order of tens of Hz, an increase of several order of magnitude compared to the shot rate achievable with state-of-the-art fusion laser technology. This rate cannot be achieved with flashlamp-pumped neodymium-doped glass lasers that require a significant interpulse cooling time. There is, presently, a very large effort to find alternative solutions [33]. We note here that the solution of the problem of thermal stability of the system for energy yield of tens of MJ/s would simultaneously provide an appropriate driver for ICF operating with ~ 2 MJ laser pulse at a repetition rate of $\mathcal{O}(10)$ Hz and, through the exploitation of CPA and the RPD acceleration mechanism described above, an unsurpassed proton acceleration facility for hadron and spallation neutron production operating at energies of ~ 1 GeV (laser pulses of 16 kJ/ε) and repetition rates of the order of a few kHz. As a purpose of illustration, Tab. 1 compares the main parameters of present and future proton drivers at the GeV energy range. The LAMPF and ISIS beam dump facilities have given neutrino sources for the LSND [34] and KARMEN [35] experiments. Currently, two projects (JAERI in Japan [36] and SNS in USA [37]) are under construction, while the European Spallation Source project (ESS) [38] and the CERN Superconducting Proton Linac (SPL) [39] are still pending approval. A RPD laser-driven acceleration facility (LAF) operating at 1 kHz and providing 10^{14} proton/pulse (i.e. with a “plate” radius of $\sim 34 \mu\text{m}$) is also shown. It corresponds to a energy yield of about 50 MJ/s at $\epsilon = 0.3$. It is a remarkable fact that the RPD acceleration mechanism allow a close synergy between the technological needs for a ICF laser driver and an ultra-intense proton driver for nuclear and particle physics applications.

3 Neutrino beams from π^+ and μ^+ decay-at-rest (DAR) and decay-in-flight (DIF)

3.1 The π^+ and μ^+ decay chains

In a neutrino beam-line based on a dump of low energy protons into a passive material, neutrinos arise from both pion and muon decays. The production of kaons or heavier mesons is negligible if the proton energy is sufficiently low ($E_p \lesssim 3$ GeV). Therefore, the neutrino beam does not suffer from ν_e and $\bar{\nu}_e$ contaminations due to kaon decays. The pion decay modes are $\pi^+ \rightarrow \mu^+ \nu_\mu$, $\pi^+ \rightarrow e^+ \nu_e$, $\pi^- \rightarrow \mu^- \bar{\nu}_\mu$ and $\pi^- \rightarrow e^- \bar{\nu}_e$ but the decays into electrons are strongly suppressed. The muon decay modes are $\mu^+ \rightarrow e^+ \nu_e \bar{\nu}_\mu$ and $\mu^- \rightarrow e^- \bar{\nu}_e \nu_\mu$. Almost all μ^+ stop before decaying and produce a Michel spectrum for ν_e and $\bar{\nu}_\mu$ while the μ^- are captured in orbit. The π^+ decay occurs both with the pion

Table 1: Main parameters of present and future proton drivers at the GeV energy range. Pot \equiv proton on target.

	Energy (GeV)	pot/pulse $\times 10^{13}$	Beam current	Repetition rate	Pulse width	Target
ISIS	0.8	2.5	200 μ A	50 Hz	100 ns	Tantalum
LAMPF	0.8	5.2	1 mA	120 Hz	600 μ s	Water/High Z
JAERI	3.0	8.3	333 μ A	25 Hz	1 μ s	Hg
SPL	2.2	15	1.8 mA	75 Hz	2.2 ms	various
SNS	1.0	15	1.4 mA	60 Hz	695 ns	Hg
ESS	1.3	84	6.7 mA	50 Hz	1.4 μ s	Hg
LAF	1.0	10	16 mA	1 kHz	<1 ps	Water/High Z

at rest, providing a mono-energetic neutrino spectrum, and in flight. The ratio DAR/DIF depends on the material and the geometry of the target. Proton-rich targets (e.g. water) are employed to obtain large pion yields. Early stopping of the mesons is achieved positioning a dense dump just after the water vessel. The distance between the water target and the stopper can be tuned to optimize the DAR/DIF ratio.

3.2 Neutrino energy spectra and beam composition

In order to estimate the expected neutrino energy spectra and beam composition, we refer to the setup of the LSND experiment, operated at LAMPF from 1993 to 1998 with 800 MeV protons impinging into a water target followed by a copper beam stopper. The precise evaluation for a laser driven facility should include the secondary yield of the nearly monochromatic distribution plus the higher energy tail (Fig. 5) and the contribution of the quasi-thermal spectrum. The former will be peaked in the 1-2 GeV range to make fully operative the RPD mechanism. The size of the latter will depend on the co-coon/plate ratio, as described in Sec. 2.2. Clearly, a precise determination of the fluxes is beyond the scope of this paper; however, we note that the use of LAMPF data implies a significant underestimation ($\sim 50\%$) of the π^+ yield and a small underestimation of the background from DIF which can be reduced through a dedicated optimization of the target-stopper distance. In the following we refer to a laser-driven facility providing 10^{14} protons-on-target (pot) per pulse at different repetition rates with a nearly monochromatic spectrum corresponding to the LSND setup⁴.

⁴Full flux calculations are available in [40]. In fact, all proposed future neutron spallation sources have as target material liquid mercury. The reason for such a choice is twofold: mercury is liquid at room temperature. Therefore, its recirculation allows a more efficient power dissipation with respect to solid

In the LSND target configuration the DAR/DIF ratio turned out to be 97%/3% [41–43]. The leading decay chain $\pi^+ \rightarrow \mu^+ \nu_\mu \rightarrow e^+ \nu_e \bar{\nu}_\mu \nu_\mu$ does not contain $\bar{\nu}_e$ and offers a unique opportunity to test the occurrence of $\bar{\nu}_\mu \rightarrow \bar{\nu}_e$ transitions. The decay of π^- might lead, in principle, to a large $\bar{\nu}_e$ contamination. However, three factors contribute to its suppression. At these proton energies, the π^+ production rate is larger than π^- by about a factor 8. Moreover, negative pions which come to rest are captured before they decay: in fact, at LAMPF, only 5% decay in orbit and, hence, contribute to the $\bar{\nu}_e$ background. Finally, almost all negative muons arising from the decays in flight come to rest in the beam dump before decaying; most then undergo the reaction $\mu^- N \rightarrow \nu_\mu e^-$ that leads to ν_μ with energy below 90 MeV, leaving only 12% of them to decay into $\bar{\nu}_e$. Hence, the relative $\bar{\nu}_e$ yield of the π^- decays at LSND, compared to the π^+ decays, is $\sim (1/8) \times 0.05 \times 0.12 \approx 7.5 \times 10^{-4}$. Clearly, the level of $\bar{\nu}_e$ contamination is much smaller than the intrinsic ν_e contamination (a few %) of a high energy ν_μ beam from π decay (e.g. the Superbeams).

The π^+ decay chain provides an intense source of monochromatic muon neutrinos ($E = 29.8$ MeV). Due to the short π^+ lifetime ($\tau_\pi \simeq 26$ ns) these neutrinos closely follow the beam time profile. This fact opens up the possibility to detect $\nu_\mu \rightarrow \nu_e$ oscillations: the $\nu_\mu \rightarrow \nu_e$ oscillations can be temporally separated from the events due to μ^+ DAR electron neutrinos, which appear on a time scale of few μ s due to the muon lifetime ($\tau_\mu \simeq 2.2$ μ s). In order to exploit the well defined time structure of a DAR beam, it is mandatory to have a proton pulse width comparable with the pion life-time. For a laser-driven facility this requirement is easily fulfilled, the proton pulse temporal spread being of the order of 1 ps.

Finally, the shape of the neutrino flux from π^+ and μ^+ decay at rest (DAR) is well known and it is shown in Fig. 6. Therefore, only the absolute amplitude has to be determined from experiments and simulation.

The simulation of the expected neutrino fluxes, both at LAMPF and ISIS, was performed by using the pion yield in proton-target interaction measured in a dedicated experiment [44]. For details on the neutrino flux simulation and the associated uncertainties we refer to [45,46]. The main source of systematic error is associated with the pion yield in proton-target interaction and it has been estimated to be about 6%. This has to be compared with the total systematic error associated to the neutrino flux from decay at rest that has been estimated to be of about 7% [45]. For neutrinos from decay in flight the

target. Moreover, the high atomic number gives a source of numerous neutrons. For neutrino applications only the first motivation holds. Indeed, high-Z elements are less efficient in producing neutrinos than low-Z elements. On the other hands, high-Z elements allow a strong suppression of DIF neutrinos. In water-based targets this suppression, if needed, can be partially recovered modifying the distance between the water vessel and the stopper.

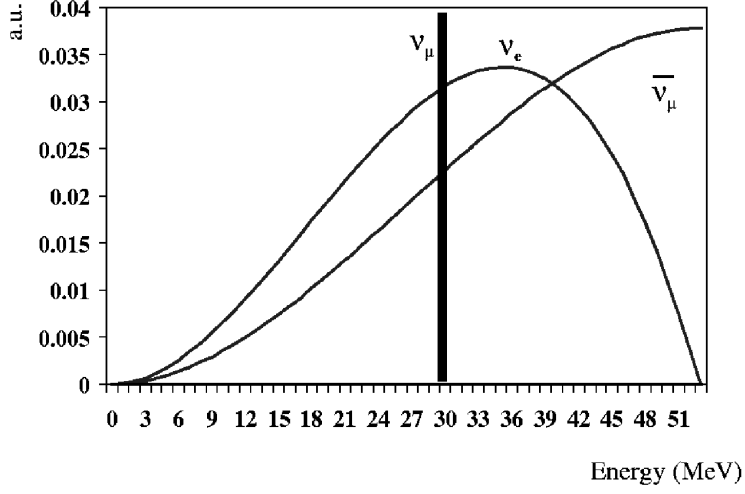


Figure 6: Neutrino energy spectra from $\pi^+ \rightarrow \mu^+ \nu_\mu \rightarrow e^+ \nu_\mu \nu_e \bar{\nu}_\mu$ decay at rest.

systematic error has been estimated to be about 15% [42].

4 The neutrino oscillation channels and the detector

In principle neutrinos from DAR and DIF decays could allow simultaneous investigation of

- $\bar{\nu}_\mu \rightarrow \bar{\nu}_e$ oscillations through the identification of DAR $\bar{\nu}_\mu$ transitions (“DAR analysis”);
- $\nu_\mu \rightarrow \nu_e$ oscillations from high energy DIF ν_μ (“DIF analysis”);
- $\nu_\mu \rightarrow \nu_e$ oscillations from DAR ν_μ temporally separated with respect to DAR ν_e (“time analysis”).

So far these channels have been used to explore neutrino oscillations at a Δm^2 of about 1 eV^2 ($E \sim 10^1 \text{ MeV}$ and $L \sim 10^1 \text{ m}$). The LSND experiment gave a positive result (there is a claim for an excess of events with an electron in the final state induced by $\bar{\nu}_\mu$ (ν_μ) oscillations into $\bar{\nu}_e$ (ν_e) [41–43]), while the KARMEN experiment gave a negative result [47]. The need for a check of these experiments caused the proposal of new projects like MiniBooNE [48] (currently data taking) and of new experiments at the Neutron Spallation Source [49]. However, there are no proposals to search with DAR and/or DIF neutrinos for oscillations at a baseline of few kilometers to test sub-dominant ν_e and

$\bar{\nu}_e$ appearance modes at the atmospheric scale. This test is unfeasible with present accelerators. Much higher intensities ($\mathcal{O}(20 \text{ mA})$ or more) are needed to overcome the large suppression due to the smallness of the ν_e CC cross-section at these energies. As noted before, a laser driven facility could offer this opportunity.

The optimization of the detector coupled with this facility is beyond the scope of this paper. Here, we will consider a detector with a technology similar to LSND and with a fiducial mass comparable with Super-Kamiokande. This corresponds to 1.3×10^{33} free protons (17 kton of CH_2). Similar detectors based on liquid scintillator have been recently proposed for low-energy neutrino astronomy and proton decay [50]. In the following, when appropriate, we refer to the LSND experimental and Monte Carlo studies to assess the physics performance of the apparatus [41–43].

The LSND detector consisted of a cylindrical tank filled with liquid scintillator. The composition was chosen to be sensitive to both Cerenkov light from electrons and relativistic muons and scintillation light from all charged particles. The light was detected through photomultiplier tubes (PMT's) covering 25% of the detector surface. PMT time and pulse-height signals were used to reconstruct the track. The Cerenkov cone for relativistic particles and the time distribution of the light, which is broader for non relativistic particles, gave excellent separation between electrons and particles below Cerenkov threshold.

5 The $\bar{\nu}_\mu \rightarrow \bar{\nu}_e$ decay at rest analysis

The search for $\bar{\nu}_\mu \rightarrow \bar{\nu}_e$ oscillations is performed by using $\bar{\nu}_\mu$ from μ^+ decay at rest. $\bar{\nu}_e$ are detected through the reaction $\bar{\nu}_e p \rightarrow e^+ n$ (plus a small contamination of $\bar{\nu}_e C \rightarrow e^+ B n$) followed by the neutron capture reaction $np \rightarrow d\gamma$, the γ energy being 2.2 MeV. A candidate $\bar{\nu}_e$ events consists in one identified electron with energy in the $20 < E_e < 60 \text{ MeV}$ range⁵ and one associated gamma. The electron identification efficiency at LSND is 42% with a relative systematic error of 7%. Note that the e^+ inefficiency is dominated by the need of vetoing Michel electrons from cosmic muons; in particular the dead-time of the veto accounts for an electron efficiency reduction of 24% [43]. The size of this background strongly depends on the shallow depth of the experimental area where LSND is located and would be significantly suppressed at deeper locations. The correlated photon is identified combining the information from the number of PMT's hits associated with the γ , its distance from the positron and the time interval between the e^+ and the γ which exploits the 186 μs delay for the neutron capture in mineral oil. The LSND analysis is based on a likelihood function R_γ whose $R_\gamma > 10$ cut corresponds to an efficiency of

⁵ β decays of cosmogenic ^{12}B prevent the use of the candidate with $E < 20 \text{ MeV}$.

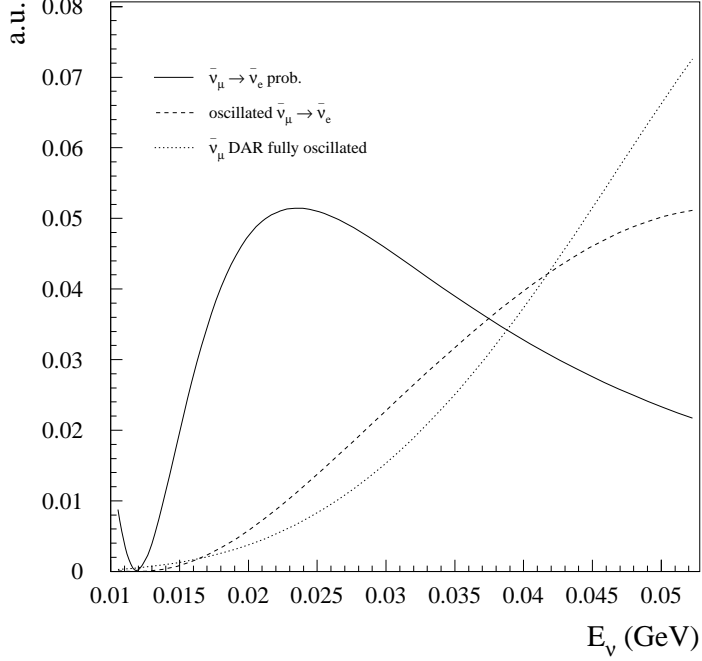


Figure 7: Energy spectrum of the fully oscillated $\bar{\nu}_\mu \rightarrow \bar{\nu}_e$ (dotted line) before the selection cuts. The two-family oscillation probability for $\Delta m^2 = 2.5 \times 10^{-3} \text{ eV}^2$ at $L = 11 \text{ km}$ (continuous line) and the corresponding convoluted $\bar{\nu}_\mu \rightarrow \bar{\nu}_e$ spectrum (dashed line) are also shown.

39% and a contamination due to accidentals at the level of 0.26%. The corresponding relative systematic uncertainty does not exceed 7%. Fig. 7 shows the energy spectrum of $\bar{\nu}_\mu \rightarrow \bar{\nu}_e$ oscillated neutrinos for 100% conversion probability before any selection cut:

$$\Phi_{\bar{\nu}_\mu}(E) \sigma_{\bar{\nu}_e p \rightarrow e^+ n}(E) \quad (23)$$

i.e. the product of the $\bar{\nu}_\mu(E)$ flux from μ^+ DAR and the $\bar{\nu}_e p \rightarrow e^+ n$ CC cross-section. The two-family oscillation probability for $\Delta m^2 = 2.5 \times 10^{-3} \text{ eV}^2$ at $L = 11 \text{ km}$ and the corresponding

$$\Phi_{\bar{\nu}_\mu}(E) \sigma_{\bar{\nu}_e p \rightarrow e^+ n}(E) P(\bar{\nu}_\mu \rightarrow \bar{\nu}_e)(E) \quad (24)$$

product is also shown. The corresponding cross-section, weighted with the DAR spectrum, is $0.95 \times 10^{-40} \text{ cm}^2$.

Contaminations to the $\bar{\nu}_e$ sample arise from beam-related interactions with neutrons in the final state, beam events without neutrons and background produced by cosmics and radioactivity (“beam unrelated”).

The main beam-related backgrounds with final state neutrons is $\bar{\nu}_e p \rightarrow e^+ n$ from μ^- decays at rest. As noted before, the μ^- DAR yield is suppressed by a factor 7.5×10^{-4} w.r.t. μ^+ DAR. The $\bar{\nu}_e p \rightarrow e^+ n$ cross-section weighted according to the $\bar{\nu}_e$ DAR spectrum is $0.72 \times 10^{-40} \text{ cm}^2$ [51]. The fraction of events with energy greater than 20 MeV is 0.806 while the electron and γ efficiencies are the same as for the signal sample. The second most important source of beam-related background events with correlated neutrons is the misidentification as $\bar{\nu}_e$ events of $\bar{\nu}_\mu p \rightarrow \mu^+ n$ CC interactions from π^- DIF. Because of the energy needed to produce a μ^+ , such a $\bar{\nu}_\mu$ must arise from a decay in flight. The final state considered are $\bar{\nu}_\mu p \rightarrow \mu^+ n$ or (less often) $\bar{\nu}_\mu C \rightarrow \mu^+ n X$, followed by $\mu^+ \rightarrow e^+ \nu_e \bar{\nu}_\mu$. In most of the cases, the muon is missed because it decays at very large times compared with $\tau_\mu \simeq 2.2 \mu\text{s}$ or the deposited energy is below the phototube threshold. The latter can occur either because the muon is too low in energy or it is produced behind the phototube surfaces. For this background, the flux weighted cross-section is $4.9 \times 10^{-40} \text{ cm}^2$, the fraction of muons in the tail of the lifetime distribution ($\tau > 12 \mu\text{s}$ or with very low kinetic energy ($T < 3 \text{ MeV}$)) is 2.6%. The positron efficiency is 42%, the fraction of events with $E > 20 \text{ MeV}$ is 81.6% and, again, the efficiency for correlated γ is 39%. Other source of misidentification are muon decays in the tail of the lifetime distribution, prompt decays to electrons so that the μ and the e are collected in a single event and muon lost by trigger inefficiencies. The whole background from μ misidentification has been computed according to the results of [43]. However, the DIF flux has been corrected keeping into account the larger distance of the detector ($L = 11 \text{ km}$ versus 30 m): at large baselines the DIF fluxes are similar to the corresponding fluxes at the center of LSND corrected for the L^{-2} suppression term.

The main source of beam related background without correlated neutrons is $\nu_e {}^{12}\text{C} \rightarrow e^- X$ scattering. The corresponding average cross-section is $1.5 \times 10^{-41} \text{ cm}^2$ [52]. For an electron reconstruction efficiency of 0.36 [41], the fraction of events with $E > 20 \text{ MeV}$ is 46% while the electron efficiency and the accidental γ efficiency at LSND are, respectively, 42% and 0.26%. Other sub-dominant sources are discussed in [41].

Beam unrelated background results mainly from unvetoesd cosmic interactions in delayed coincidence with accidental photons. It strongly depends on the veto quality, the depth of the detector and the rate of accidental photons. Moreover, it can be suppressed if the duty cycle of the beam is sufficiently low. For the case of LSND, the poor time structure of the beam and the shallow depth of the detector does not allow an effective suppression of this background, which is estimated during the beam-off data taking and,

hence, subtracted. On the other hand, the time structure of ISIS allows a suppression of more than two order of magnitude compared with LSND in the $\bar{\nu}_\mu \rightarrow \bar{\nu}_e$ channel, so that KARMEN does not suffer from this contamination. For the laser-driven facilities considered here the time structure is very well defined (see Sec. 2 and [18]) and the beam-off background could be non negligible (at the depth of LSND) only for very high repetition rates (~ 10 kHz). At larger depths, this contamination is negligible for any realistic repetition rate and, hence, it is not considered in the present analysis.

6 Sensitivity to θ_{13}

In order to get information about the magnitude and phase of the U_{e3} term of the PMNS mixing matrix, terrestrial experiments explore sub-dominant effects in the neutrino transition probabilities at the atmospheric scale which, in general, are suppressed by at least one power of $\alpha \equiv \Delta m_{21}^2 / |\Delta m_{23}^2|$ ⁶. Since matter effects are negligible for baselines of the order of $L = 10$ km, the $\nu_\mu \rightarrow \nu_e$ oscillation probability can be expressed as [53]:

$$\begin{aligned} P(\nu_\mu \rightarrow \nu_e) &\simeq \sin^2 2\theta_{13} \sin^2 \theta_{23} \sin^2 \Delta \\ &- \alpha \sin 2\theta_{13} \sin \delta \cos \theta_{13} \sin 2\theta_{12} \sin 2\theta_{23} \sin^3 \Delta \\ &- \alpha \sin 2\theta_{13} \cos \delta \cos \theta_{13} \sin 2\theta_{12} \sin 2\theta_{23} \cos \Delta \sin^2 \Delta \\ &+ \alpha^2 \cos^2 \theta_{23} \sin^2 2\theta_{12} \sin^2 \Delta \\ &\equiv O_1 + O_2 + O_3 + O_4, \end{aligned} \quad (25)$$

Δ being the oscillation phase $\Delta m_{23}^2 L / 4E_\nu$ in natural units ($c = \hbar = 1$). If the energy and the baseline of the experiment is chosen to fulfill $\Delta \simeq \pi/2$ (oscillation maximum), the O_3 term is suppressed. Similarly, the term O_4 can be neglected unless $\sin^2 2\theta_{13} \simeq \mathcal{O}(10^{-4})$. Hence, the $\nu_\mu \rightarrow \nu_e$ transition probability can be expressed in the simplified form:

$$\begin{aligned} P(\nu_\mu \rightarrow \nu_e) &\simeq \sin^2 2\theta_{13} \sin^2 \theta_{23} \sin^2 \Delta \\ &- \alpha \sin 2\theta_{13} \sin \delta \cos \theta_{13} \sin 2\theta_{12} \sin 2\theta_{23} \sin^3 \Delta \end{aligned} \quad (26)$$

Its CP conjugate $\bar{\nu}_\mu \rightarrow \bar{\nu}_e$ is therefore

$$\begin{aligned} P(\bar{\nu}_\mu \rightarrow \bar{\nu}_e) &\simeq \sin^2 2\theta_{13} \sin^2 \theta_{23} \sin^2 \Delta \\ &+ \alpha \sin 2\theta_{13} \sin \delta \cos \theta_{13} \sin 2\theta_{12} \sin 2\theta_{23} \sin^3 \Delta \end{aligned} \quad (27)$$

and a simultaneous measurement of ν_e and $\bar{\nu}_e$ gives access⁷ to the magnitude and phase of the U_{e3} entry.

⁶A global analysis of all available neutrino oscillation data gives for α a best fit value of 0.026, while the 3σ allowed range is $0.018 < \alpha < 0.053$ [6].

⁷This determination is not unique due to the $\delta \rightarrow \pi - \delta$ and $\theta_{23} \rightarrow \pi/2 - \theta_{23}$ invariance of the transition probabilities [54,55].

The analysis described in Section 5 allows a determination of $P(\bar{\nu}_\mu \rightarrow \bar{\nu}_e)$. To ease comparison with other proposed facilities, we interpret $P(\bar{\nu}_\mu \rightarrow \bar{\nu}_e)$ assuming no CP violation in the leptonic sector ($\delta = 0$), $\theta_{23} = \pi/4$ and $\Delta m_{23}^2 = 2.5 \times 10^{-3} \text{ eV}^2$, so that

$$P(\bar{\nu}_\mu \rightarrow \bar{\nu}_e) \simeq \sin^2 2\theta_{13} \sin^2 \theta_{23} \sin^2 \Delta$$

$$= \frac{1}{2} \sin^2 2\theta_{13} \sin^2 \left[1.27 \frac{\Delta m_{23}^2 (\text{eV}^2) L (\text{km})}{E (\text{GeV})} \right] \quad (28)$$

and performing a two parameter fit of Δm_{23}^2 and $\sin^2 2\theta_{13}$. The fluxes of $\bar{\nu}_\mu$ from π^+ DAR are computed for a facility providing 10^{14} pot/pulse with variable repetition rates. The π^+ yield considered here is $0.09 \pi^+/\text{pot}$, corresponding to the LSND setup [45]. As discussed in Sec. 3.2, this estimate is rather conservative for a laser-based facility. In 5 years of data taking, assuming 6 months of operation and 50% beam on time, the overall integrated flux at 11 km is $2.3 \times 10^7 \times R \nu/\text{cm}^2$, R being the repetition rate in Hz. At $R = 1 \text{ kHz}$, we expect 473 $\bar{\nu}_e$ CC events assuming 100% $\bar{\nu}_\mu \rightarrow \bar{\nu}_e$ conversion rate. The corresponding background is below 0.6 events (0.28 from μ^- DAR, 0.16 from π^- DIF with the muon misidentified and 0.16 from events without correlated γ). The systematic errors for signal and background are inferred from the LSND analysis and shown in Table 2. Fig. 8 shows the 90% confidence level (CL) exclusion limit for $\sin^2 2\theta_{13}$ in the occurrence of the null hypothesis ($\theta_{13} = 0$) as a function of the repetition rate. The corresponding sensitivities coming from the $\nu_\mu \rightarrow \nu_e$ appearance search for MINOS [56], CNGS [57], JPARC-SK [9] and JPARC to Hyper-Kamiokande [9] are also shown, together with the present CHOOZ [2] limit from $\bar{\nu}_e$ disappearance. The two-parameter exclusion region at 90% CL for a 10 kHz facility is depicted in Fig. 9.

7 $\nu_\mu \rightarrow \nu_e$ appearance searches

In LSND $\nu_\mu \rightarrow \nu_e$ oscillations were searched for by exploiting the ν_μ flux from decay in flight. As discussed in Section 3, about 3% of the π^+ decay in flight originating a ν_μ beam with average energy of about 90 MeV. ν_e are detected through the reaction $\nu_e e \rightarrow e X$ and requiring the electron to have energy in the range $60 \div 200 \text{ MeV}$. The corresponding value of the cross-section for $\langle E_\nu \rangle \sim 9 \text{ MeV}$ is about $15 \times 10^{-40} \text{ cm}^2$ [52], i.e. a factor 15 larger than $\bar{\nu}_e$ inverse β -decay (see Section 5). Taking into account the different detection efficiencies [42] we expect a ratio of fully oscillated DIF/DAR events of about one third with a signal to noise ratio comparable to both analyzes. Note, however, that the energy of DIF neutrinos does not match the maximum of the oscillation probability for the baseline considered ($L = 11 \text{ km}$ for $\Delta m_{23}^2 = 2.5 \times 10^{-3} \text{ eV}^2$).

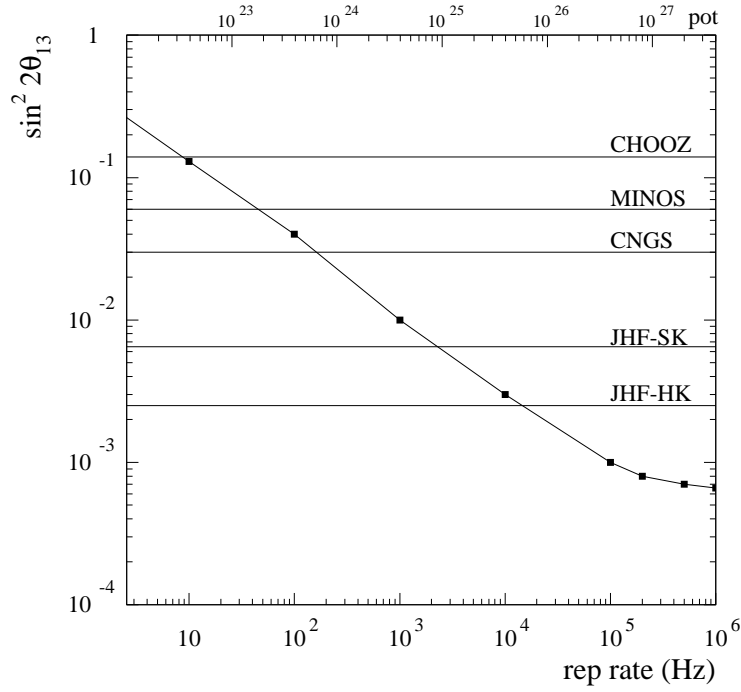


Figure 8: Exclusion limit at 90% CL for $\sin^2 2\theta_{13}$ (two parameter fit) as a function of the repetition rate. The corresponding integrated protons on target for 5y of data taking are also shown. The horizontal bands indicate the corresponding limit from $\nu_\mu \rightarrow \nu_e$ appearance search at MINOS, CNGS, JPARC to Super-Kamiokande and JPARC to Hyper-Kamiokande; the upper band shows the present CHOOZ limit from $\bar{\nu}_e$ disappearance search.

Table 2: Breakdown of systematic errors for the $\bar{\nu}_\mu \rightarrow \bar{\nu}_e$ DAR analysis.

Channel	Source	Error (%)
signal	flux	7
	cross-sec	-
	eff	7
	γ id	7
$\bar{\nu}_e$ from DAR μ^-	flux	15
	cross-sec	-
	eff	7
	γ id	7
$\bar{\nu}_\mu$ from DIF π^-	flux	15
	eff + cross-sec	41
	γ id	7
ν_e ^{12}C from DAR μ^+	inclusive	17

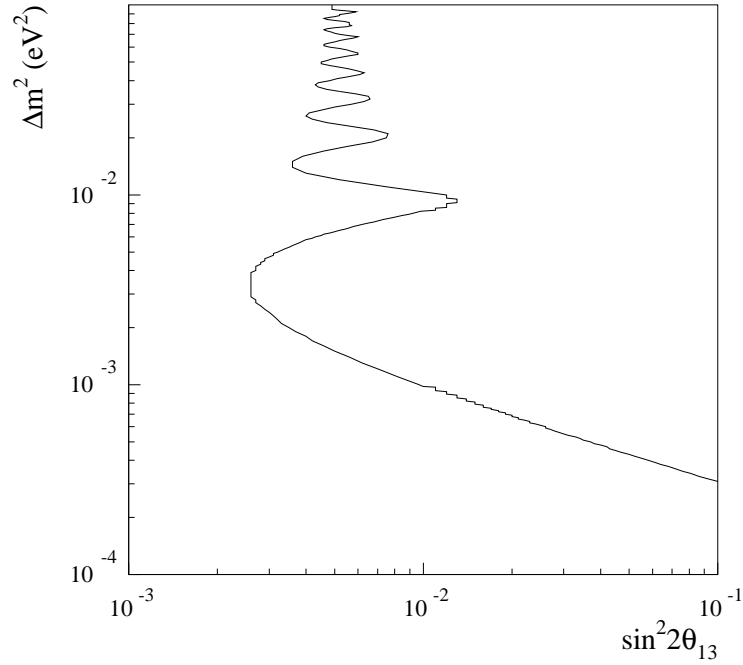


Figure 9: Exclusion limit at 90% CL in the $(\Delta m_{23}^2, \sin^2 2\theta_{13})$ plane for 10 kHz repetition rate.

The time analysis searches for $\nu_\mu \rightarrow \nu_e$ oscillations by looking for mono-energetic ν_e ($E_\nu = 29.8$ MeV) in a short time window after the proton pulse. The length of the time window is determined by the pion life-time ($\tau_\pi = 26$ ns). The ν_e are detected through the CC reaction of ν_e onto ^{12}C giving rise to an electron and a ^{12}N (ground state) followed by the β -decay $^{12}\text{N}_{g.s.} \rightarrow ^{12}\text{C} e^+ \nu_e$ with 15.9 ms decay time. This analysis was found particularly appealing for the following reasons: the main background is induced by ν_e from fast μ^+ -decay within the time window, but can be precisely measured and subtracted; due to $\nu_e ^{12}\text{C} \rightarrow e^- ^{12}\text{N}_{g.s.}$ interactions from μ^+ decays outside the time window, the full oscillation expectation is normalized by the experiment itself. However, the sensitivity of this channel is essentially limited by the small cross-section of the involved reaction (4.95×10^{-42} cm², at $E_\nu = 29.8$ MeV, to be compared with the inverse β -decay reaction whose cross-section is 0.95×10^{-40} cm², convoluted over the whole DAR spectrum). Summarizing the search for $\nu_\mu \rightarrow \nu_e$ oscillations is very interesting for CP-violation studies, but it is not at the peak of the oscillation probability in the DIF analysis ($E/L \sim 0.1$ GeV/11 km $\sim 10^{-2}$; $\Delta \sim 0.34$) and it is limited by statistics in the time analysis. The impact of this channel on CP-violation studies is currently under investigation and will be the subject of a forthcoming paper.

8 Conclusions

The current debate for multipurpose facilities aimed at high precision studies of neutrino oscillations drove the authors towards the study of non-conventional neutrino sources. In particular, we noted that the possibility to accelerate efficiently protons in the GeV energy range through relativistic laser-plasma interactions opens up interesting opportunities for the development of a new generation of proton drivers. In this paper we discussed a radiation pressure dominated (RPD) mechanism for relativistic proton acceleration. This mechanism is highly efficient compared to previous proposals and could allow a close synergy between present R&D finalised to energy production through inertial confined fusion and the wealth of applications related to high intensity multi-GeV drivers (see Appendix). Moreover, we demonstrated that this facility could allow for the first time the study of subdominant $\nu_\mu \rightarrow \nu_e$ oscillations at the atmospheric scale with neutrinos produced by π^+ decays at rest or in flight.

Acknowledgements

We wish to thank S. Atzeni, M. Borghesi, A. Donini, J. Koga, K. Nishihara, A. V. Titov, M. Yamagiwa for many useful suggestions and A. Pakhomov for interesting discussions

at the early stage of this work. A special thank to P. Strolin for encouragement and advice on the potentiality of future proton drivers.

Appendix

In the last decade, interest towards the construction of high intensity proton drivers in the few GeV range has steadily grown. The main reason is connected with the wide range of applications that can be simultaneously accessed by these facilities. The most intense neutron beams (spallation sources) are currently produced by bombarding mercury targets with energetic protons from a large few-GeV proton accelerator complex. As it is well known, applications range from chemistry to crystalline and disordered materials studies, superconductivity, polymers and structural biology investigations. A discussion of the physics case for intense spallation sources can be found in [58]. A wide physics program is accessible in neutrino physics, beyond the oscillation issues discussed above [49]. The availability of a high power, high duty factor proton beam could provide opportunities in stopped muon physics, in search for rare decays as $\mu \rightarrow e\gamma$, $\mu \rightarrow eee$ or muon conversion $\mu N \rightarrow eN$, and improvements in muon decay properties. The neutrino energy range is appropriate for neutrino-nucleus cross section measurements of relevance to supernova astrophysics: dynamics, nucleosynthesis and terrestrial supernova ν detection. Similarly, measurements of neutrino-nucleus cross sections open the possibility to study interesting nuclear structure issues related to the weak interaction as the ratio of the axial to vector coupling constants and the search for non-standard contributions. Finally it's worth noting that oscillation studies at the $\Delta m^2 \sim 1 \text{ eV}^2$ scale will become a major priority in ν physics in case of confirmation of the LSND ν_e appearance claim.

References

- [1] Y. Fukuda *et al.* [Super-Kamiokande Coll.], Phys. Rev. Lett. **81** (1998) 1562; Y. Ashie *et al.* [Super-Kamiokande Coll.], Phys. Rev. Lett. **93** (2004) 101801; M. Ambrosio *et al.* [MACRO Coll.], Phys. Lett. B **517** (2001) 59; M. Sanchez *et al.* [Soudan 2 Coll.], Phys. Rev. D **68** (2003) 113004; B.T. Cleveland *et al.*, Astrophys. J. **496** (1998) 505; J.N. Abdurashitov *et al.* [SAGE Coll.], Phys. Rev. C **60** (1999) 055801; W. Hampel *et al.* [GALLEX Coll.], Phys. Lett. B **447** (1999) 127; S. Fukuda *et al.* [Super-Kamiokande Coll.], Phys. Rev. Lett. **86** (2001) 5651; Q.R. Ahmad *et al.* [SNO Coll.], Phys. Rev. Lett. **87** (2001) 071301; K. Eguchi *et al.* [KamLAND Coll.], Phys. Rev. Lett. **90** (2003) 021802; M.H. Ahn *et al.* [K2K Coll.], Phys. Rev. Lett. **90** (2003) 041801.

- [2] M. Apollonio *et al.* [CHOOZ Coll.], Eur. Phys. J. C **27** (2003) 331.
- [3] F. Boehm *et al.* [PALO VERDE Coll.], Phys. Rev. D **64** (2001) 112001.
- [4] Z. Maki, M. Nakagawa, S. Sakata, Prog. Theor. Phys. **28** (1962) 870; B. Pontecorvo, Sov. Phys. JETP **26** (1968) 984.
- [5] K. Hagiwara *et al.* [Particle Data Group Collaboration], Phys. Rev. D **66** (2002) 010001.
- [6] M. Maltoni, T. Schwetz, M. A. Tortola, J. W. F. Valle, Phys. Rev. D **68** (2003) 113010.
- [7] S. Geer, Phys. Rev. D **57** (1998) 6989 [Erratum-ibid. D **59** (1999) 039903]; A. De Rujula, M. B. Gavela and P. Hernandez, Nucl. Phys. B **547** (1999) 21.
- [8] P. Zucchelli, Phys. Lett. B **532** (2002) 166.
- [9] Y. Itow *et al.*, KEK-REPORT-2001-4, arXiv:hep-ex/0106019.
- [10] M. V. Diwan *et al.*, Phys. Rev. D **68**, 012002 (2003).
- [11] A. Maksimchuck *et al.*, Phys. Rev. Lett. **84** (2000) 4108; E. L. Clark *et al.*, Phys. Rev. Lett. **85** (2000) 1654; S. P. Hatchett *et al.* Phys. Plasmas **7** (2000) 2076; R. A. Snavely *et al.*, Phys. Rev. Lett. **85** (2000) 2945; A. J. Mackinnon *et al.*, Phys. Rev. Lett. **86** (2001) 1769; M. Hegelich *et al.*, Phys. Rev. Lett. **89** (2002) 085002.
- [12] I. Spencer *et al.*, Nucl. Instr. Meth. B **183** (2001) 449.
- [13] M. Borghesi *et al.*, Plasma Phys. Control. Fusion **43** (2001) A267.
- [14] T. Tajima, J. Jpn. Soc. Therap. Rad. Oncol. **9** (1998) 83; C. Ma *et al.*, Med. Phys. **28** (2001) 1238; S.V. Bulanov, V.S. Khoroshkov, Plasma Phys. Rep. **28**, (2002) 453; S. V. Bulanov *et al.*, Phys. Lett. A **299** (2002) 240.
- [15] K. Krushelnik *et al.*, IEEE Trans. Plasma Sci. **28** (2000) 1184.
- [16] T. Tajima, G. Mourou, Phys. Rev. Special Topics Accelerators and Beams **5** (2002) 031301-1.
- [17] T. Zh. Esirkepov, M. Borghesi, S. V. Bulanov, G. Mourou, T. Tajima, Phys. Rev. Lett. **92** (2004) 175003.

- [18] A. V. Pakhomov, J. Phys. G **28** (2002) 1469.
- [19] V. Yu. Bychenkov, Y. Sentoku, S. V. Bulanov, K. Mima, G. Mourou, S. V. Tlokonnikov, JETP Lett. **74** (2001) 664.
- [20] S. V. Bulanov, T. Zh. Esirkepov, J. Koga, T. Tajima, Plasma Phys. Rep. **30** (2004) 196.
- [21] V. I. Veksler, in Proceedings of CERN Symposium on High Energy Accelerators and Pion Physics, Geneva, Vol. 1, p. 80, 1956; At. Energy **2** (1957) 427.
- [22] S. V. Bulanov *et al.*, in Reviews of Plasma Physics. Vol.22, p. 227, V.D. Shafranov ed., Kluwer Academic/Plenum Publishers, New York, 2001.
- [23] R. Bingham, J. T. Mendonca, P. K. Shukla, Plasma Phys. Control. Fusion **46** (2004) R1.
- [24] D. Umstadter, J. Phys. D: Appl. Phys. **36** (2003) R151.
- [25] L. D. Landau, E. M. Lifshitz, The Classical Theory of Fields, Pergamon Press, Oxford, 1980.
- [26] V. F. D'yachenko, V. S. Imshennik, Sov. J. Plasma Phys. **5** (1979) 413; F. Brunel, Phys. Rev. Lett. **59** (1987) 52; Phys. Fluids **31** (1988) 2714.
- [27] T. Zh. Esirkepov, Comput. Phys. Comm. **135** (2001) 144.
- [28] K. Matsukado *et al.*, Phys. Rev. Lett. **91** (2003) 215001.
- [29] T. Utsumi, K. Matsukado, H. Daido, T. Zh. Esirkepov, S. V. Bulanov, Appl. Phys. A **79** (2004) 1185.
- [30] I. N. Ross, *et al.*, Optics Commun. **144** (1997) 125.
- [31] G. Mourou, T. Tajima, S. V. Bulanov, Rev. Mod. Phys. (2004) in press.
- [32] D. Strickland, G. Mourou, Optics Commun. **56** (1985) 219.
- [33] E.L. Saldin *et al.*, Fus. Eng. and Design **44** (1999) 341; Y. Kitagawa *et al.*, Fus. Techn. **21** (1992) 1460; S. B. Sutton *et al.*, AIAA Journal **30** (1992) 431; C. D. Orth *et al.*, Nucl. Fus. **36** (1996) 75; For a general discussion see also <http://www.llnl.gov/str/Payne.html>; J.D. Sethian *et al.*, Nucl. Fus. **43** (2003) 1693.

- [34] C. Athanassopoulos *et al.* [LSND Collaboration], Nucl. Instrum. Meth. A **388** (1997) 149.
- [35] H. Gemmeke *et al.* [KARMEN Collaboration], Nucl. Instrum. Meth. A **289** (1990) 490.
- [36] Details on the JAERI neutron spallation source are available at <http://jkj.tokai.jaeri.go.jp/> ; W. Chou, “Spallation Neutron Source and Other High Intensity Proton Sources”, Lecture at the 3rd OCPA International Accelerator School, Singapore, July 25 - August 3, 2002, arXiv:physics/0301025; Y. Yamasaki *et al.*, ”High-intensity proton accelerators for the JAERI/KEK Joint Project”, Proc. 2000 European Accel. Conf., THOAF201 (2000).
- [37] Details on the SNS neutron spallation source are available at <http://www.sns.gov/>
- [38] “ESS A Next Generation Neutron Source for Europe”, Vol. 1-3, The ESS Feasibility Study, March 1997. Details are available at <http://www.ess-europe.de/>
- [39] B. Autin *et al.*, “Conceptual design of the SPL, a high-power superconducting H-linac at CERN,”, Yellow Report CERN-2000-012.
- [40] Details on the flux calculations at LAMPF can be found at <http://www.phys.lsu.edu/~sung/lsnd/beammc/>
- [41] C. Athanassopoulos *et al.* [LSND Collaboration], Phys. Rev. C **54** (1996) 2685.
- [42] C. Athanassopoulos *et al.* [LSND Collaboration], Phys. Rev. C **58** (1998) 2489.
- [43] A. Aguilar *et al.* [LSND Collaboration], Phys. Rev. D **64** (2001) 112007.
- [44] R. C. Allen *et al.*, Nucl. Instrum. Meth. A **284** (1989) 347.
- [45] R. L. Burman, M. E. Potter, E. S. Smith, Nucl. Instrum. Meth. A **291** (1990) 621.
- [46] R. L. Burman, Nucl. Instrum. Meth. A **368** (1996) 416.
- [47] B. Armbruster *et al.* [KARMEN Collaboration], Phys. Rev. D **65** (2002) 112001.
- [48] I. Stancu *et al.* [MiniBooNE collaboration], FERMILAB-TM-2207.
- [49] F.T. Avignone, L. Chatterjee, Y.V. Efremenko, M. Strayer (eds.), Proc. of the Workshop on Neutrino Studies at the Spallation Neutron Source, J. Phys. G **29** (2003) 2497.

- [50] L. Oberauer, Mod. Phys. Lett. A **19** (2004) 337.
- [51] C. H. Llewellyn Smith, Phys. Rep. **3** (1972) 262; P. Vogel, Phys. Rev. D **29** (1984) 1918; P. Vogel, J. F. Beacom, Phys. Rev. D **60** (1999) 053003.
- [52] E. Kolbe, K. Langanke, S. Krewald, Phys. Rev. C **49** (1994) 1122.
- [53] A. Cervera *et al.*, Nucl. Phys. **B579** (2000) 17, erratum *ibid.* Nucl. Phys. **B593** (2001) 731; M. Freund, Phys. Rev. **D64** (2001) 053003.
- [54] J. Burguet-Castell *et al.*, Nucl. Phys. B **608** (2001) 301.
- [55] V. Barger, D. Marfatia, K. Whisnant, Phys. Rev. D **65** (2002) 073023.
- [56] M. V. Diwan, Nucl. Phys. Proc. Suppl. **123** (2003) 272.
- [57] M. Komatsu, P. Migliozi, F. Terranova, J. Phys. G **29** (2003) 443
- [58] J. Finney (ed.), “The Scientific-strategic Case for a Next generation European Spallation Neutron Source for Science and Research (ESS Project)”, Dec. 2000.